JOM, Vol. 77, No. 4, 2025
https://doi.org/10.1007/s11837-025-07128-1

In Situ Neutron Diffraction Study of Strain Evolution and Load Partitioning During Elevated Temperature Tensile Test in HIP-Treated Electron Beam Powder Bed Fusion Manufactured Ti-6Al-4V

K. PANDIAN ,[1,6] M. NEIKTER,[1] M. EKH,[1,3] S. HARJO,[4] T. KAWASAKI,[4] R. WORACEK,[5] T. HANSSON,[1,2] and R. PEDERSON[1]

1.—Department of Production Technology, University West, 461 86 Trollhättan, Sweden. 2.—GKN Aerospace Engine Systems, 461 38 Trollhättan, Sweden. 3.—Department of Industrial and Materials Science, Chalmers University, 412 96 Gothenburg, Sweden. 4.—J-PARC Center, Japan Atomic Energy Agency, Ibaraki, Tokai 319-1195, Japan. 5.—European Spallation Source, 224 84 Lund, Sweden. 6.—e-mail: karthikeyan.thalavai-pandian@hv.se

To manufacture almost fully dense components, electron beam powder bed fusion of Ti-6Al-4V is typically combined with post-heat treatment, such as hot isostatic pressing (HIP). The standard HIP treatment performed at 920°C and 100 MPa for 2 h results in coarsening of the microstructure and impacting the yield strength. A low-temperature HIP treatment performed at 800°C and 200 MPa for 2 h resulted in limited coarsening and comparable yield strength to as-built material. A coarser microstructure is detrimental to tensile properties. Tensile testing at different temperatures revealed that thermal activation of different slip systems could possibly affect the elongation behavior, demanding additional investigation. Performing in situ neutron time of flight diffraction during tensile testing provides data to analyze strain evolution and load partitioning in the crystal lattice, which includes the slip planes. A two-phase elastic–plastic self-consistent model has been used to analyze and compare the experimental results. The lattice strain evolution results indicated that the basal slip {0 0 0 2} was activated at 20°C while the pyramidal slip {1 0 $\bar{1}$ 1} was first activated during loading at 350°C. Load partitioning results showed that the β phase endures higher stresses than the α phase in the plastic regime.

INTRODUCTION

In the last decade, additive manufacturing (AM) has been widely recognized as an alternate manufacturing process over conventional methods due to reduced material wastage and shorter lead times.[1,2] Over the years, the manufacturing of Ti-6Al-4V using electron beam powder bed fusion (PBF-EB), a powder bed fusion AM technique, has evolved as a promising process.[3–5] The resulting microstructure and defect distribution in PBF-EB are affected by the different process parameters, which impact the mechanical properties.[6] Typically, materials manufactured by PBF-EB are subjected to post-processing operations such as hot isostatic pressing (HIP) treatment to close defects and improve fatigue properties.[7] Standard HIP treatments are performed below the β transus temperature, resulting in coarser microstructure and reduced yield strength.[4,8] A previous study reported that HIP treatment performed at 800°C and 200 MPa for 2 h resulted in limited coarsening and better yield strength than standard HIP treatment (920°C and 100 MPa for 2 h).[9] The elevated temperature tensile performance of such low-temperature HIP-treated Ti-6Al-4V was evaluated earlier.[10] The results from the study[10] indicated that the effect of temperature

(Received July 11, 2024; accepted January 2, 2025; published online January 28, 2025)

on material elongation could be related to thermal-based activation of slip systems, which needs further investigation.

Ti-6Al-4V is an $\alpha + \beta$ alloy with a high phase volume fraction of hexagonal closed pack (HCP) α phase and a small volume fraction of body center cubic (BCC) β phase (typically $< 10\%$) at room temperature.[11] The deformation mechanisms in Ti-6Al-4V can occur in both phases,[12] but the slip in the HCP α phase mostly dominates the mechanical properties because of its large volume fraction.[13] Plastic deformation in an HCP system occurs through the different slip planes, namely basal {0 0 0 2}, prismatic {1 0 $\bar{1}$ 0}, and pyramidal {1 0 $\bar{1}$ 1}, in the shortest Burger vector direction $< a >$.[12] More slip systems that are needed to meet the von Mises yield criterion are provided by the deformation in the $< c + a >$ direction and twinning.[14] The Burger vectors are comparatively longer for the $< c + a >$ direction. Consequently, the slip along the $< a >$ direction is most favored due to less energy required for slip movement.[15] In $\alpha + \beta$ alloys, such as Ti-6Al-4V, the deformation twinning is largely suppressed due to the high alloy content and small phase dimensions.[12] So, the most active slip systems in Ti-6Al-4V are the {0 0 0 2}, {1 0 $\bar{1}$ 0}, and {1 0 $\bar{1}$ 1} planes in the $< a >$ direction. One of these three slip systems becomes the primary active slip system when the resolved shear stress on the specific slip plane in the slip direction reaches a critical value. Temperature is one of the factors that affects the critically resolved shear stress (CRSS) value of a slip system. As a result, different slip systems are activated in the individual grains depending on temperature.[16]

To determine the CRSS and the active slip system, different techniques can be utilized. Slip trace analysis using electron backscattered diffraction (EBSD) and transmission electron microscopy (TEM) have been widely adopted to study the activation of slip systems in titanium alloys.[17,18] An alternate method is X-ray or neutron diffraction measurements combined with elastic–plastic self-consistent (EPSC) modeling. Turner and Tome[19] were the first to successfully obtain the CRSS values of different HCP slip systems in Zircaloy-2 using neutron diffraction and EPSC simulations. The approach has been developed further and investigated for other HCP materials such as titanium alloys.[20,21] Stapleton et al.[22] used X-ray diffraction combined with EPSC simulations to investigate the evolution of lattice strains in Ti-6Al-4V. Sofinowski et al.[23] studied the strain evolution in PBF-EB manufactured and post-heat-treated Ti-6Al-4V using in situ X-ray diffraction.[23] Several publications have reported applying neutron diffraction to analyze the texture in PBF-EB Ti-6Al-4V.[24–27] To the best of the authors' knowledge, limited work has been performed to utilize neutron diffraction and EPSC models to investigate strain evolution in different HIP-treated PBF-EB Ti-6Al-4V.

In the present study, the main objective is to understand the effect of temperature on the activation of various slip systems in different HIP-treated PBF-EB Ti-6Al-4V. In situ tensile tests performed with and without heating combined with neutron diffraction measurements will help determine the lattice strain evolution. It has been shown that the evolution of lattice strains can depict load shedding occurring in the soft oriented grains and load transfer occurring in plastically hard oriented grain families.[28,29] Further, the diffraction data have been assessed with the EPSC model to compare and gain more confidence with the experimental results.

MATERIALS AND METHOD

Materials

The samples were manufactured in an ARCAM Q20 plus PBF-EB machine with 50 μm thick layer running a 5.3.76 process theme. Standard plasma atomized Ti-6Al-4V powder from AP&C (Canada) having a particle size distribution of 45–105 μm was used to produce the samples. The PBF-EB-manufactured samples were subjected to standard (920°C, 100 MPa, 2 h) and modified (800°C, 200 MPa, 2 h) HIP treatments in a Quintus QIH 21 M URC equipment in Västerås (Sweden). The different types of the HIP-treated samples were machined at Metcut Research (USA) to a gauge length of 36 mm and gauge diameter 6 mm.

In Situ Tensile Testing with Neutron Diffraction

The neutron time of flight (ToF) measurements were performed with the TAKUMI instrument at the Japan proton accelerator research complex (j-PARC). The instrument was equipped with a load frame capable of performing tensile tests up to a load of 50 kN, and the specimen axis was oriented 45° to the incident beam. The test rig was fitted with a furnace to perform the elevated temperature tensile tests. The test was carried out under displacement control mode in the elastic and plastic regime. An extensometer was attached to the specimens to measure the axial strain. The standard and modified HIP-treated specimens were tested at 20 and 350°C with a 0.005 ± 0.002 mm/mm/min strain rate. Figure 1 shows a schematic of the instrument layout and images of the instrument set-up showing the extensometer and furnace heating. The loading direction indicated in Fig. 1 is along the build direction (BD) of the specimen. The neutron flux on the sample was 4.8×10^7 n/s/cm^2 (high-intensity mode) with a resolution of 0.4%. A slit of 7 mm $\times$ 5 mm was used to restrict the incident neutron beam and obtain bulk diffraction measurements in the specimen gauge section. The

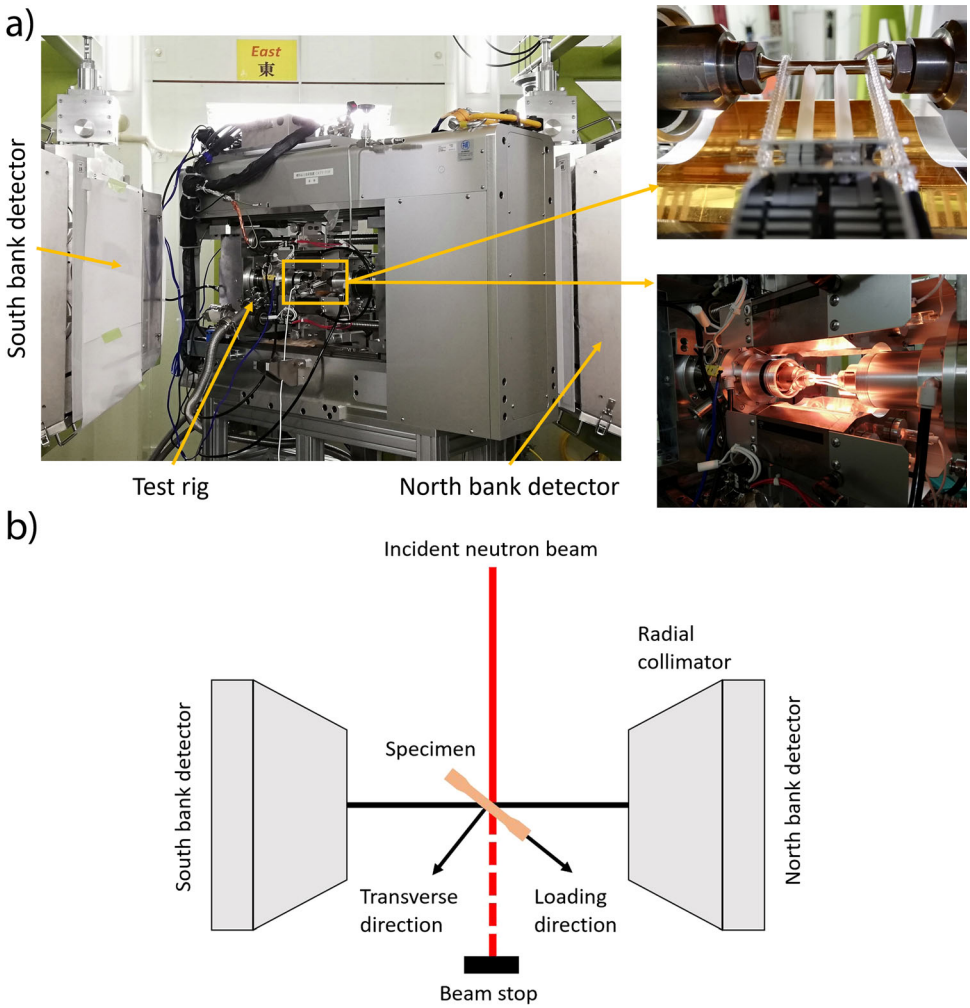

Fig. 1. Neutron ToF instrument set-up: (a) *left* the test rig placed at 45° orientation to the incoming beam from the east direction and the two detectors in the south and north to acquire the diffractions in transverse and loading directions, respectively; *top right* the sample fitted with a strain gauge; *bottom right* the specimen heated with a furnace during the elevated temperature tensile test. (b) Schematic of the neutron diffraction instrument.

set-up had two detector banks located at angles 90° to the incident neutron beam, enabling simultaneous measurement of lattice strains along the loading direction (north bank) and perpendicular to the applied load (south bank). The d-spacing range was fixed between 0.5 and 2.7 Å, enabling the possibility of acquiring the entire diffraction pattern for each detector. Rietveld analysis of the entire diffraction pattern was performed using the software, Z-Rietveld version 1.1.3.[30]

Figure 2 shows the macroscopic stress–strain curve from in situ tests performed at 20°C and 350°C in the neutron diffraction instrument. The test was interrupted at specific load and strain levels to acquire the neutron diffraction measurements, as shown in Fig. 2 (points shown by TOF diffraction data). Each of the ToF diffraction measurements was obtained in 10 min. The ToF data points in Fig. 2 represent the diffraction measurements used to investigate the evolution of lattice strains and load partitioning between different phases.

The neutron ToF method combines De Brogile's equation and Bragg's law to connect the ToF diffraction pattern with d-spacing, as shown in:

$$\lambda = \frac{ht}{mL} = 2d \sin\theta \tag{1}$$

where λ is the wavelength, h is Planck's constant, t is the ToF, m is the mass of the neutron, L is the neutron path length, d is the interplanar spacing, and θ is the Bragg angle.

The interplanar spacing for different hkl planes has been obtained from the diffraction pattern by Rietveld refinement performed in the Z-Rietveld software. Rietveld refinement is a powerful technique to refine the position, shape, and intensities of multiple Bragg peaks in the diffraction pattern by generating a calculated profile that fits the experimental data. Rietveld method uses a non-linear

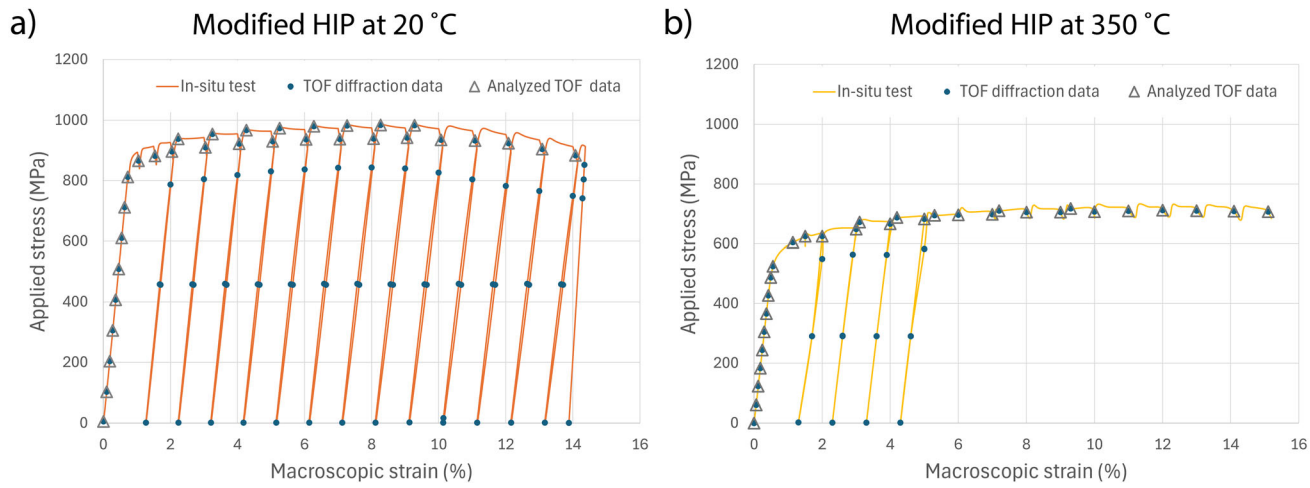

Fig. 2. The macroscopic stress–strain data acquired by in situ tensile test at (a) 20°C and (b) 350°C for modified HIP-treated material. The in situ test was performed in the neutron diffraction instrument, and the TOF data points represent the test interruptions for neutron diffraction measurements. The analyzed ToF *data points* indicate the diffraction measurements used for the strain evolution and load partitioning investigations.

least squares minimization approach to perform the fitting between the observed (experimental) profile and the calculated profile. As the position, shape, and intensity of the Bragg peaks are connected to the material crystal properties by fitting the Bragg peaks, it is possible to relate the interplanar spacing of different *hkl* planes to the respective Bragg peaks in the diffraction pattern.

Next, the lattice strain (ε_{hkl}) was calculated from Eq. 2 by determining the interplanar spacing for a particular $\{d_{hkl}\}$ plane from the refined diffraction pattern during deformation and a reference interplanar spacing (d^o_{hkl}) for the same plane in undeformed material condition:

$$\varepsilon_{hkl} = \frac{(d_{hkl} - d^o_{hkl})}{d^o_{hkl}} \qquad (2)$$

The load partition between the different phases was obtained from the EPSC model. The phase fraction for the α and β phases has been obtained by integrating the area under intensity peaks for the respective phases using the Pawley refinement method in the software tool, Z-Rietveld.

Metallographic Investigation

A scanning electron microscope (SEM; GeminiSEM 450; ZEISS) equipped with an EBSD detector (Symmetry; Oxford) was utilized to obtain the pole figures for texture analysis. An acceleration voltage of 15 kV, a step size of 3 μm, and a magnification of × 150 were used to obtain sufficient interaction volume and broad area coverage. The inverse pole figures and the pole figures were obtained by processing the EBSD data in AZtecCrystal (version 3.1).

Elastic–Plastic Self-Consistent Modeling

EPSC models provide a basic framework to model the mechanics of polycrystalline materials. The essential advantage of using the EPSC model is that it is a computationally efficient way of calculating stresses and strains in all the individual grains as well as the homogenized stresses and strains. The mathematical content of this EPSC model has been developed from the model described in the literature.[31–33] Both the α and β phases in the present model have 5000 grains with a random texture, as researchers have reported random texture in PBF-EB-manufactured Ti-6Al-4V.[24,26] The EBSD measurements from the current study also indicate a weak texture in the material, as explained in Sect. "Pole Figures." The EPSC model has been defined by the elastic parameters, such as the elastic stiffness matrix constants, C_{ij}, listed in Table I, and the lattice constants, c and a, for the HCP crystal. Components of the stiffness matrix for the two phases were fitted by adjusting the initial values from the literature using the EPSC model. The components of the stiffness matrix for the α phase were fitted to the elastic part of the lattice strains (see Fig. 5) by adjusting the initial values from the literature using the EPSC model, the components for the β phase were obtained directly from the literature[22] and were assumed to be the same for 350°C. This simplification is motivated by the low volume fraction of the β phase, which makes it difficult to determine the parameter values since their influence on the response is limited. The Vocé hardening parameters listed in Table II were obtained by calibration against the experimental data. In the second step of the calibration, the Vocé hardening parameters listed in Table II and critical resolved shear stress in Table IV (see below) were

Table I. Elastic constants (MPa) for the α phase (fitted) and β phase (obtained from22) used in the EPSC model

Sample	Phases	C_{11}	C_{12}	C_{13}	C_{33}	C_{44}
Modified HIP at 20°C	α	180700	100610	77408	198400	45541
Modified HIP at 350°C	α	170925	105702	80651	193402	45310
Modified HIP at 20°C	β	130000	90000	90000	130000	65000
Modified HIP at 350°C	β	130000	90000	90000	130000	65000

Table II. Vocé hardening parameters used to fit the plastic strains in the EPSC model

	Vocé hardening parameters (MPa)					
	{1 0$\bar{1}$ 0} Prismatic		{0 0 0 2} Basal		{1 0 $\bar{1}$ 1} Pyramidal	
Parameters	Modified HIP at 20°C	Modified HIP at 350°C	Modified HIP at 20°C	Modified HIP at 350°C	Modified HIP at 20°C	Modified HIP at 350°C
τ_1	15.7	18.2	15.4	15.5	14.6	17.7
θ_0	162.2	175.1	162.2	175.1	162.2	175.1
θ_1	50.0	50.0	50.0	50.0	50.0	50.0

obtained by calibration against both the full macroscopic stress–strain data and the lattice strains.

RESULTS

Pole Figures

The pole figures for the modified and standard HIP-treated samples representing the HCP α phase slip planes {1 0 $\bar{1}$ 0}, {0 0 0 2}, and {1 0 $\bar{1}$ 1} along with the multiples of random distribution (MRD) values are shown in Fig. 3. The {0 0 0 2} basal slip plane reported the highest MRD values of 7.40 and 7.14 for the modified and standard HIP-treated samples, respectively. However, considering that the reported MRD values were from EBSD measurements, the values are relatively low, indicating weak texture in the material.

Rietveld Refinement

The diffraction patterns acquired from the experiment were fitted using the inbuilt peak model function in the Z-Rietveld software. Ti-6Al-4V belongs to space group 194, and its α phase has lattices with a length of 0.295 nm and a height of 0.468 nm, while the β phase has a lattice parameter of 0.332 nm. The lattice parameters of both phases were refined using the Pawley method, and the calculated volume phase fractions are reported in Table III. The diffraction peaks were analyzed in the *d*-spacing range of 1.2–2.7 Å, as this study mainly focused on the evolution of strains in the slip planes. Figure 4 shows a diffraction spectrum in the transverse direction after Rietveld analysis observed in the undeformed and deformed condition of the modified HIP-treated specimen tested at 20°C. The respective lattice planes for diffraction peaks in each phase are indicated in Fig. 4. The peaks corresponding to the slip planes are marked with an asterisk. The lattice planes with limited peak intensity that had challenges in extracting accurate lattice parameters are represented in italics in Fig. 4a. The shifting of the peaks, corresponding to the slip planes, can be visualized in Fig. 4b with the help of black dotted lines representing the d-spacing of the respective planes in the undeformed condition. It is noteworthy that the Bragg peaks also show broadening when the material is deformed.

Evolution of Lattice Strains

Figure 5 shows the lattice strain evolution during the in situ tensile test for the selected slip planes in the α phase of standard and modified HIP-treated material tested at 20°C and 350°C. The diffraction peaks analyzed from both the detectors (loading and transverse directions) are plotted in Fig. 5. The plot shows that each slip mode has a linear elastic response followed by a deflection from linearity. This vertical deflection from linearity represents the load shedding (unloading) of the slip mode. In contrast, the deflection from linearity on the horizontal direction indicates load getting transferred into the respective family of planes. The deflection from linearity that represents load shedding is indicated by black arrow in Fig. 5a–d. For the samples tested at 20°C, the vertical deflection from linearity first occurred in the {0 0 0 2} diffraction plane in the loading direction at about 800 MPa for modified HIP-treated material and about 700 MPa in standard HIP-treated material. For the samples

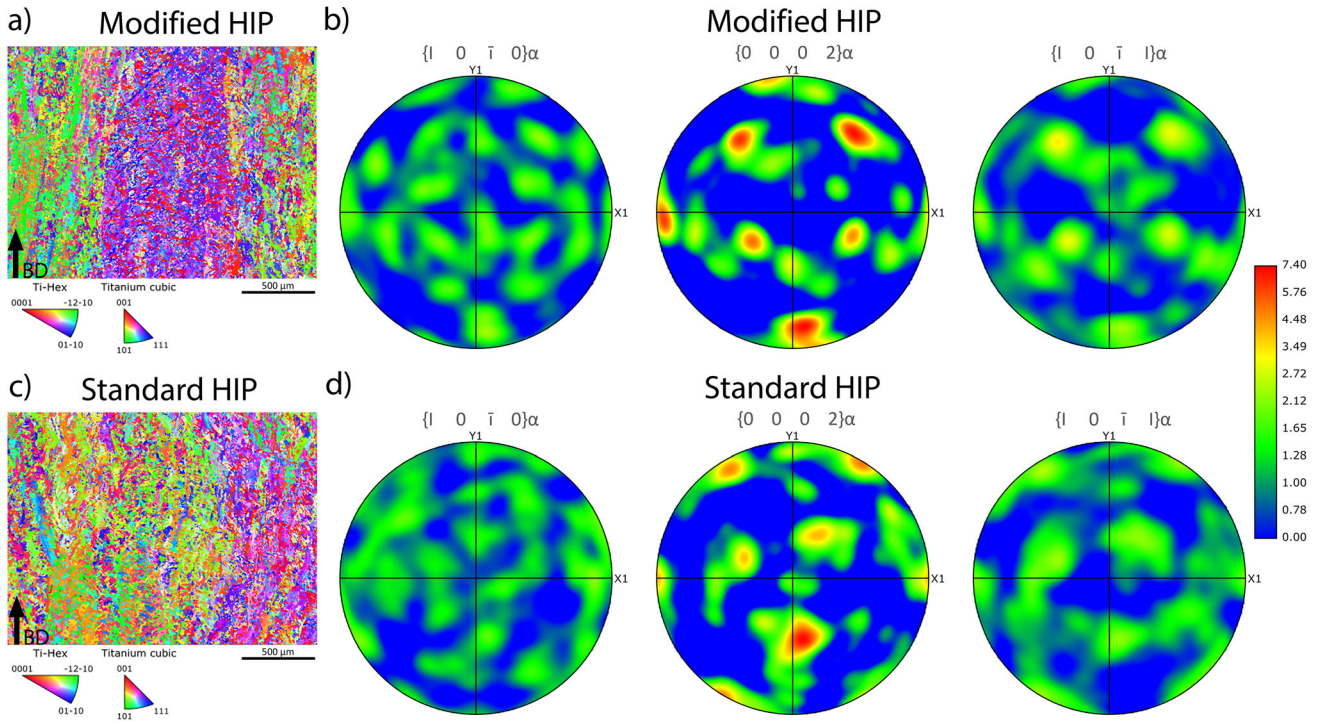

Fig. 3. Overview of the inverse pole figures along the build direction (BD) are shown for (a) modified HIP-treated and (c) standard HIP-treated samples. The pole figures of prismatic, basal, and pyramidal slip planes in the HCP α phase are shown for (b) modified HIP-treated and (d) standard HIP-treated samples. The *colour codes* in (b) and (d) represent MRD values. *X* and *Y* are in plane along the BD.

Table III. Volume phase fraction of the standard and HIP-treated material calculated from the diffraction data

	Volume phase fraction (%)					
	α phase (HCP)			β phase (BCC)		
Material	**Loading direction**	**Transverse direction**	**Average**	**Loading direction**	**Transverse direction**	**Average**
Standard HIP	91.0	91.6	91.3 ± 0.008	9.0	8.4	8.7 ± 0.008
Modified HIP	95.3	95.6	95.5 ± 0.006	4.7	4.4	4.6 ± 0.006

tested at 350°C, in the loading direction the deflection from linearity starts in the {1 0 $\bar{1}$ 1} diffraction plane at about 500 MPa in modified HIP-treated material and at about 400 MPa in standard HIP-treated material. Figure 5d shows that other diffraction planes, {0 0 0 2} and {1 0 $\bar{1}$ 0}, also deflected from linearity at about 400 MPa.

In Figs. 6 and 7, the lattice strain evolution from the diffraction peak data and the EPSC two-phase model simulations are compared for modified HIP-treated material tested at 20°C and 350°C, respectively. It can be observed from Fig. 6 that the model predictions are in good agreement with the experimental results except for the β phase, particularly in the elastic region. Figure 7 also shows that the simulations are in good agreement with the experimental values for the α phase slip modes. The CRSS values of the modified HIP material tested at 20°C and 350°C for the three HCP slip modes are listed in Table IV, in which the {0 0 0 2} (basal) slip mode has the lowest CRSS value, followed by the {1 0 $\bar{1}$ 0} (prismatic) and {1 0 $\bar{1}$ 1} (pyramidal) slip modes for materials tested at 20 and 350°C. The elastic modulus values measured from the diffraction experiment and calculated from the EPSC model for the modified HIP-treated material tested at 20°C and 350°C are shown in Table V. The elastic modulus values indicate that there is a good agreement between the experiment and simulation results.

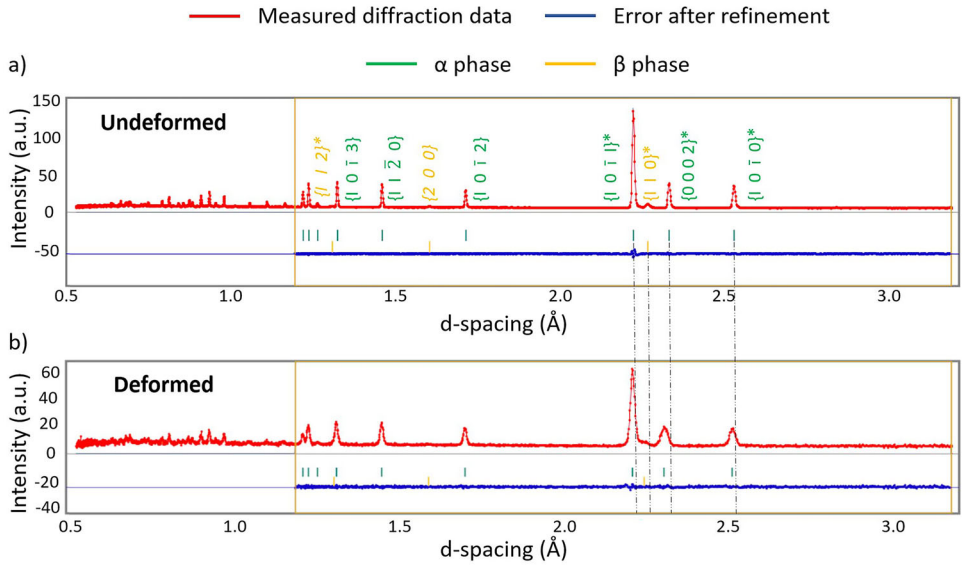

Fig. 4. Diffraction spectra in the transverse direction of the modified HIP-treated specimen tested at 20°C after Rietveld refinement: (a) undeformed condition and (b) after deformation. The lattice peaks marked with * are the slip planes. The lattice planes {200} and {112} with too little intensity to derive lattice parameters are indicated in italics. The *dashed black line* references *d*-spacing in the undeformed condition for the investigated slip planes.

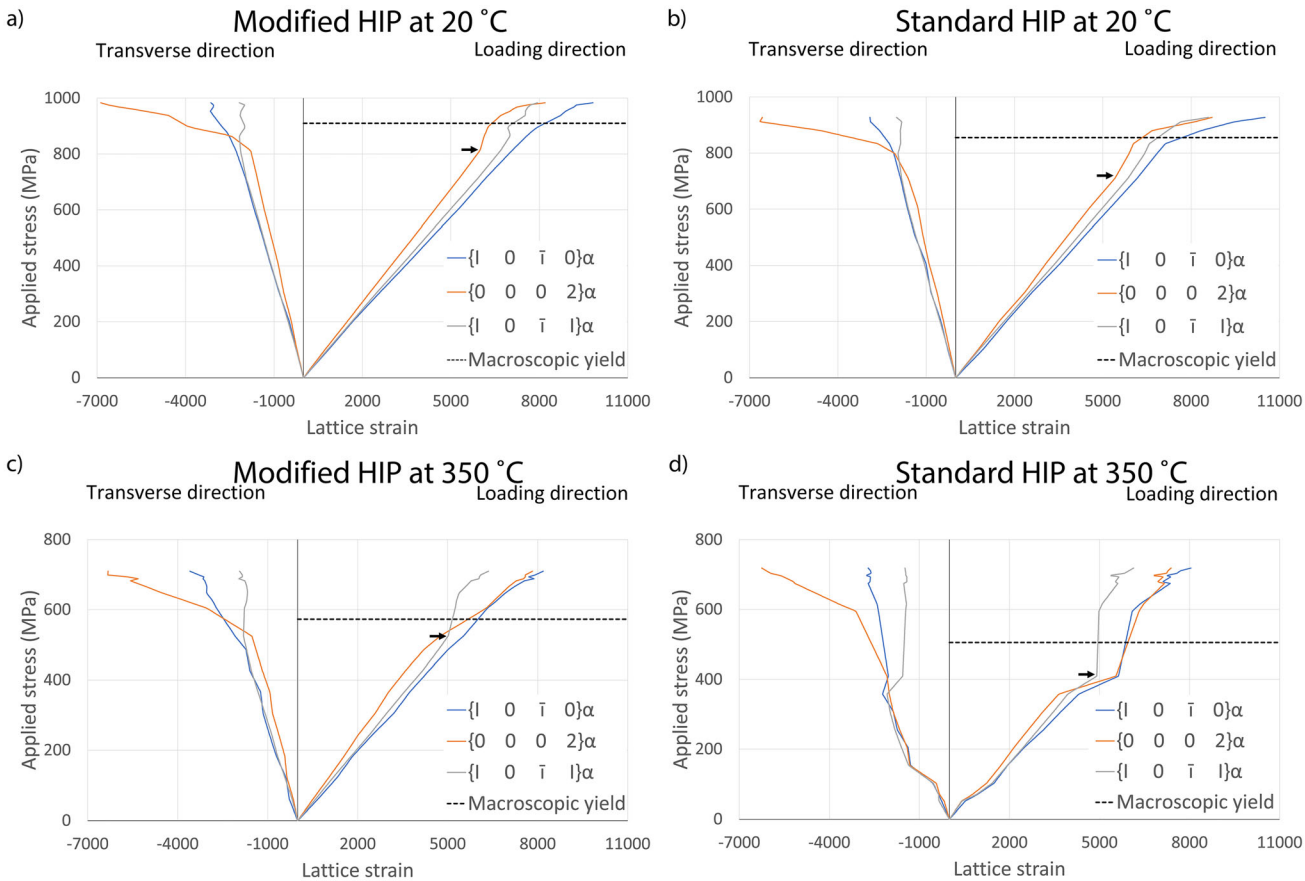

Fig. 5. Evolution of lattice strains in the HCP planes from in situ tensile tests: (a) modified HIP-treated material at 20°C, (b) standard HIP-treated material at 20°C, (c) modified HIP-treated material at 350°C, and (d) standard HIP-treated material at 350°C; *black arrow* indicates the load shedding in the diffraction planes.

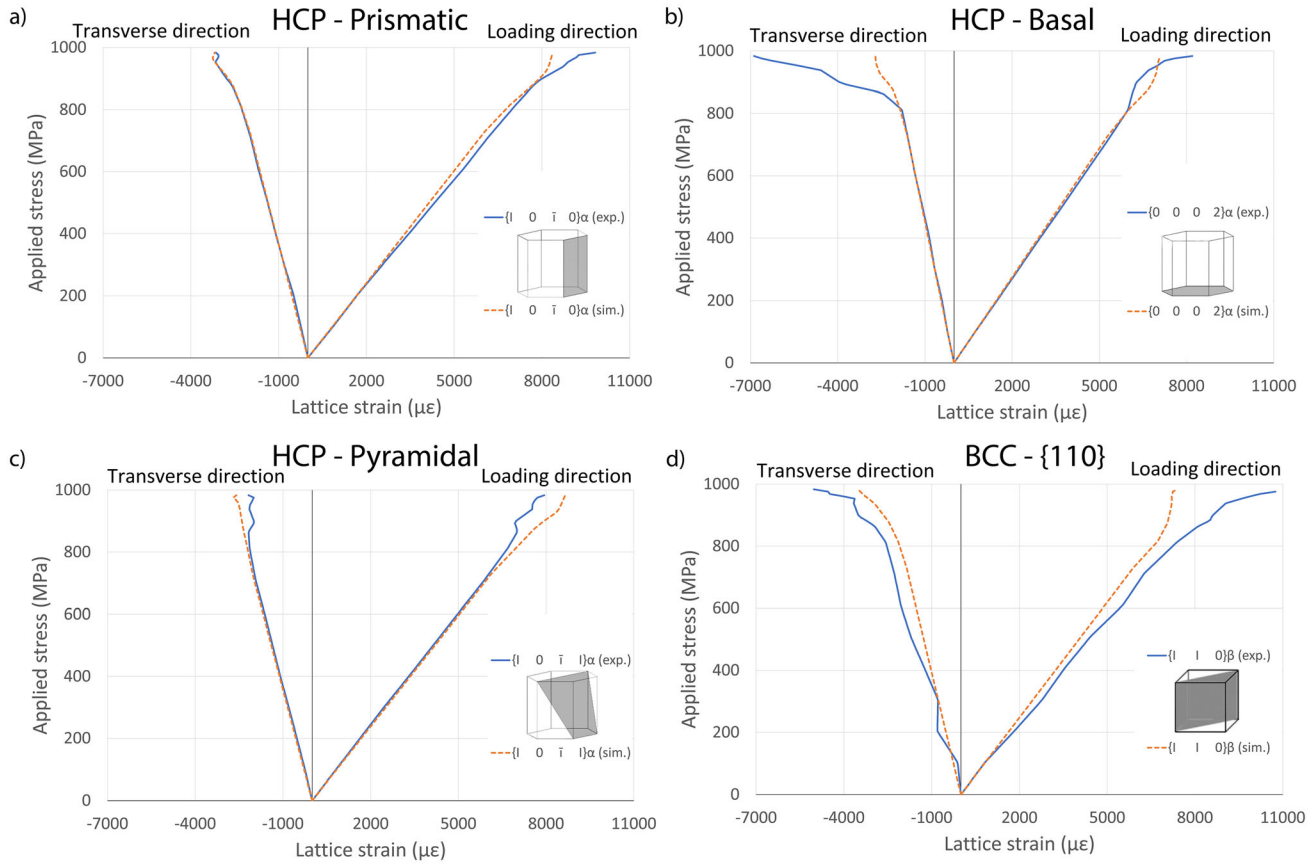

Fig. 6. Comparison between in situ tensile tests and EPSC simulations of lattice strains along the (a) prismatic, (b) basal, and (c) pyramidal slip planes in the HCP α phase, and (d) the {110} slip planes in the BCC β phase for modified HIP-treated material tested at 20°C.

Load Partitioning Between Phases at Room Temperature

Figure 8 shows the stress–strain plots for modified HIP-treated material tested at room temperature. The simulation results are compared with the experimental data in Fig. 8a and the load portioning between α and β phases is shown in Fig. 8b. The stresses in the α and β phases were obtained from the EPSC model predictions. The stress–strain plots from the model predictions align closely with the experimental curves. Further, the load sharing between the two phases indicates higher stresses for the β phase than for the α phase in the plastic region.

DISCUSSION

Lattice Strain Evolution

The micromechanical behavior of the HIP-treated materials tested at different temperatures can be analyzed from the lattice strain evolution plots shown in Fig. 5. Stress (σ) versus ε_{hkl} curves at 20°C show almost linearity in the initial stages of the lattice strain evolution, depicting elastic behavior in the material, the difference in slope between the planes indicating elastic anisotropy, i.e., basal is stiffer than pyramidal, which in turn is stiffer than the prismatic plane. Figure 5a and Table V show that, for modified HIP-treated materials in the elastic regime, the {0 0 0 2} family of planes are stiffer by $\sim$ 12% than the {1 0 $\bar{1}$ 1} family of planes, which in turn are stiffer by $\sim$ 6% than the {1 0 $\bar{1}$ 0} family of planes. Similarly, Fig. 5b and Table V show that, for standard HIP-treated materials in the elastic regime, the {0 0 0 2} family of planes are stiffer by $\sim$ 10% than the {1 0 $\bar{1}$ 1} family of planes, which in turn are stiffer by $\sim$ 4% than the {1 0 $\bar{1}$ 0} family of planes. The vertical deviation from linearity occurs at different slip modes well before the macroscopic yield points, which are 910 MPa and 855 MPa at 20°C for modified and standard HIP-treated material, respectively. The macroscopic yield points for modified and standard HIP-treated materials at 350°C are 573 MPa and 505 MPa, respectively. The plastically soft grain families undergo load shedding and transfer the load to the other plastically hard grain families until the macroscopic yield point is reached.[23] The simulation results of the HCP slip modes in Figs. 6 and 7 show that the EPSC model can reasonably predict the behavior of load transfer and load shedding in the lattice planes. However, at larger elastic strains after yielding, the fit is in general not that good. The exact reason must be further investigated in future,

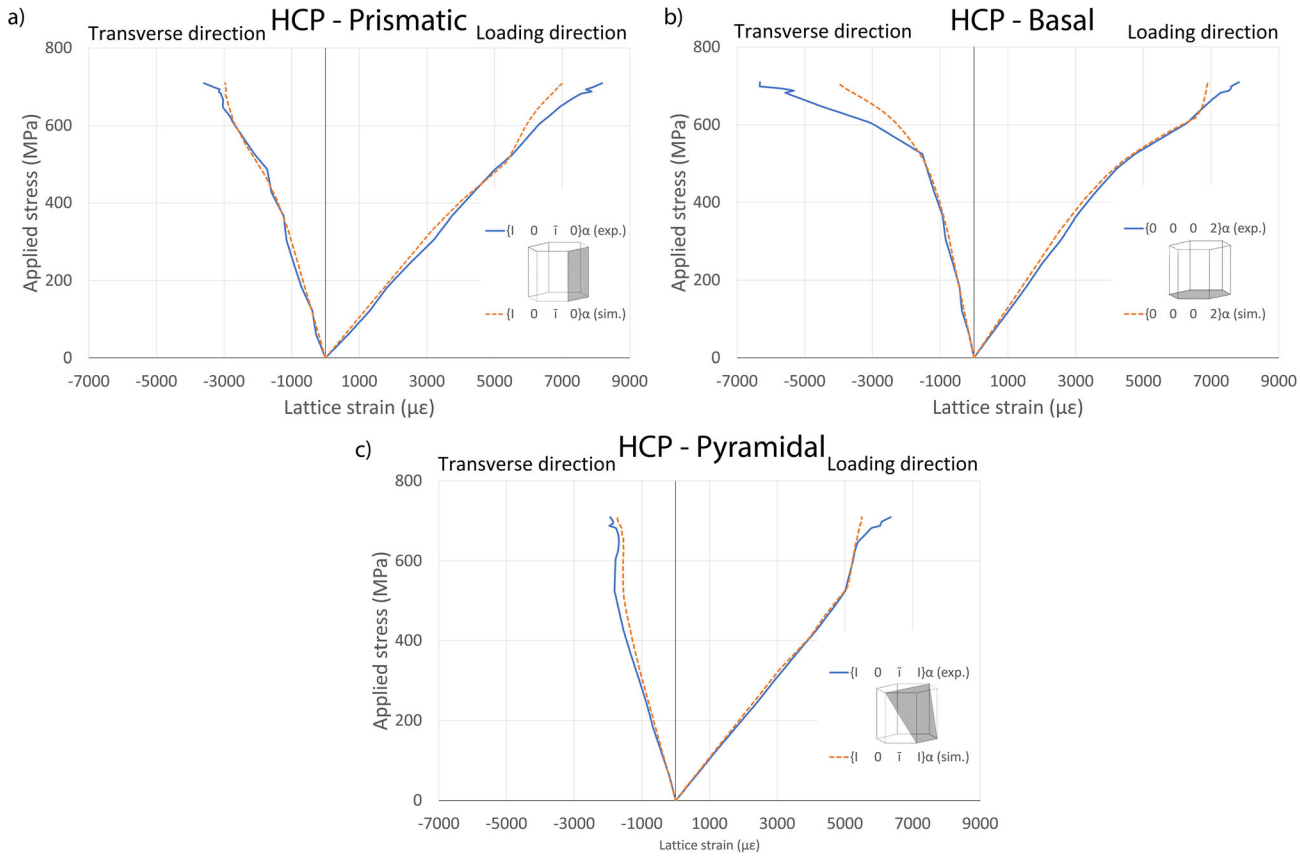

Fig. 7. Comparison between in situ tensile tests and EPSC simulations of lattice strains along the (a) prismatic, (b) basal, and (c) pyramidal slip planes for modified HIP-treated material tested at 350°C.

Table IV. Critical resolved shear stresses of the different slip modes in the HCP obtained from the EPSC model

	Critical resolved shear stress (MPa)		
Sample and test condition	**{1 0 $\bar{1}$ 0} Prismatic**	**{0 0 0 2} Basal**	**{1 0 $\bar{1}$1} Pyramidal**
Modified HIP at 20°C	388.4	319.7	479.5
Modified HIP at 350°C	199.3	155.3	238.7

Table V. Experimental and simulated diffraction elastic modulus (GPa) for modified HIP-treated material tested at 20 and 350°C

Temperature	**20°C**			**350°C**		
Diffraction peaks	**{I 0 $\bar{1}$ 0} Prismatic**	**{0 0 0 2} Basal**	**{I 0 $\bar{1}$I} Pyramidal**	**{I 0 $\bar{1}$ 0} Prismatic**	**{0 0 0 2} Basal**	**{I 0 $\bar{1}$ I} Pyramidal**
E_{hkl} (exp.)	114.2	134.9	120.5	98.2	119.4	102.8
E_{hkl} (sim.)	120	137	118.5	104	124.7	100.4

but it is believed that the hardening model should be improved to account more physical mechanisms.[22] Further, in the selected BCC slip plane {110}, the model predictions were found to be less in agreement with the experimental values, which is believed to be due to its low phase fraction.

Britton et al.[15] reported that, among HCP materials, at room temperature, the slip preferably occurs in the {0 0 0 2} slip plane in materials with an ideal c/a ratio of 1.633. As the {0 0 0 2} slip plane is the most densely packed in the HCP system, it is the most preferred plane for the slip to occur.[34]

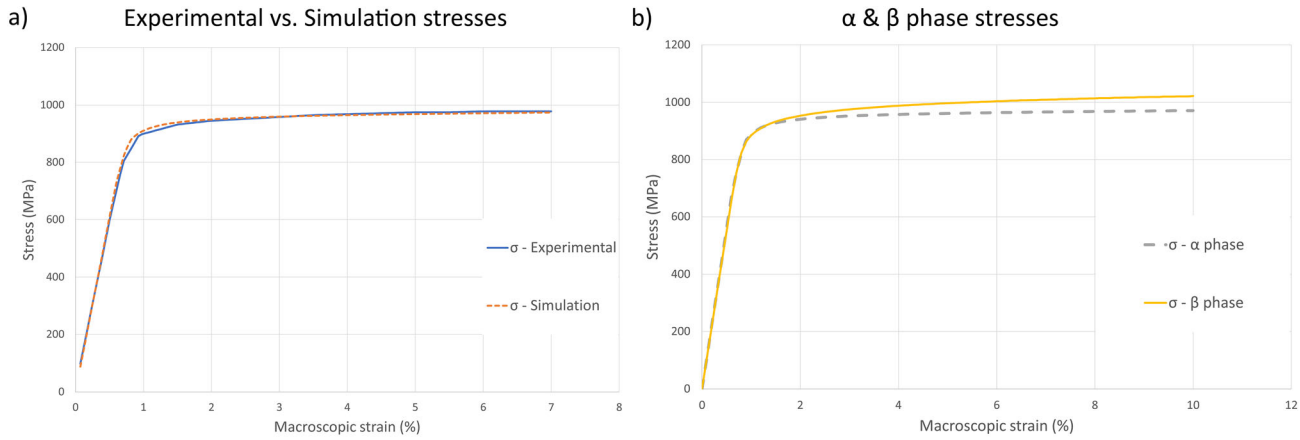

Fig. 8. Stress–strain plots of modified HIP-treated material tested at room temperature: (a) comparison of the EPSC model predictions with experimental data, and (b) load partitioning between phases.

However, when the *c*/*a* ratio decreases from the ideal value, the relative ease for slip to occur transfers from {0 0 0 2} to {1 0 $\bar{1}$ 0}. In the case of pure titanium with a *c*/*a* ratio of 1.588, the {1 0 $\bar{1}$ 0} plane is mostly the primary active slip plane at room temperature.[15] In pure titanium single crystals, the CRSS value at which plastic deformation occurs is about three times higher for the {0 0 0 2} slip than for the {1 0 $\bar{1}$ 0} slip at room temperature.[35] The difference in CRSS between the {0 0 0 2} and {1 0 $\bar{1}$ 0} slips is reduced when the percentage of interstitial elements such as Al becoming higher. Consequently, both the {0 0 0 2} and {1 0 $\bar{1}$ 0} slip systems can be equally important to become activated in TiAl alloys with a 6.6% Al concentration.[36] In the current study, it was observed that the {0 0 0 2} diffraction plane was activated at room temperature.

In the case of materials tested at 350°C, deflection from linearity occurred at a lower stress value in all the HCP slip modes than at room temperature, which was as expected. Figure 5c along the loading direction shows that a vertical deflection of lattice strain occurs in the {1 0 $\bar{1}$ 1} diffraction plane indicating that this plane has plastically soft orientation. On the other hand, load transfer occurs in the {0 0 0 2} and {1 0 $\bar{1}$ 0} diffraction planes, as these planes have a plastically hard orientation. In the case of single-crystal Ti-6.6Al, the CRSS of the {1 0 $\bar{1}$ 1} system was observed to be far higher than the {0 0 0 2} and {1 0 $\bar{1}$ 0} systems at room and elevated temperatures.[36] However, an earlier study on the bimodal Ti-6Al-4V showed that the {1 0 $\bar{1}$ 1} slip was highly activated at temperatures above 275°C, although the reason for such an activation mechanism needs to be explored.[37] Further results from Wang et al.[38] have also shown activation of the {1 0 $\bar{1}$ 1} system for welded bimodal Ti-6Al-4V in the temperature range between 150°C and 300°C. Figure 5d along the loading direction shows that vertical deflection of lattice strain occurs simultaneously in the {1 0 $\bar{1}$ 1}, {0 0 0 2}, and {1 0 $\bar{1}$ 0} diffraction planes. However, there is a sudden increase in the lattice strains in all three diffraction planes just before deflection, so there could be other mechanisms involved that need to be studied further.

It has been considered that the high solute content in $\alpha + \beta$ titanium alloys suppresses deformation by twinning.[12] However, in conventionally manufactured Ti-6Al-4V, deformation twining has been observed during uniaxial compression at low strain rates.[39] Also, Ti-6Al-4V manufactured by laser powder bed fusion deformed by tensile and compression twinning, in addition to the slip mode deformation during uniaxial compression at low strain rates.[40] Deformation-induced tensile and compression twins were also observed for PBF-EB Ti-6Al-4V samples during uniaxial tensile test, particularly in samples having coarser α lath thickness ($\sim$ 0.6 μm).[41] The HIP-treated materials investigated in the current study have an α lath thickness greater than 0.6 μm,[10] so the material can exhibit deformation twinning. Typically, the {1 0 $\bar{1}$ 1} and {1 1 $\bar{2}$ 2} twins were identified as compression twins in HCP materials, and in titanium the {1 0 $\bar{1}$ 1} twinning becomes activated at elevated temperatures.[42] Figure 5d shows a decrease of lattice strain in the {1 0 $\bar{1}$ 1} plane in the transverse direction between $\sim$ 350 MPa and 400 MPa. This sudden reduction in lattice strain in the transverse direction is accompanied by lattice strain changes in the loading direction, indicating a possible activation of twinning. In general, a sudden change in lattice strain for a small change in applied stress indicates possible twinning behavior.[43] However, in Fig. 5d, a sudden change in strain occurred in all three diffraction planes but only in loading direction for stresses $<$ 75 MPa, so there could be an other physical phenomenon occurring other than twinning that needs further investigation. In the current work, there are limited data available to come to any conclusion about other physical

phenomena inducing a sudden change in lattice strain. Still, one possible phenomenon that could affect the lattice strain at 350°C for Ti-6Al-4V can be creep mechanism. Further investigation of lattice strain evolution during creep loading will help to clarify this hypothesis.

Phase Volume Fraction and Load Partitioning Between Phases

The phase volume fractions reported in Table III shows that the β phase volume fractions were about 9% and 5% for the standard HIP-treated and modified HIP-treated materials, respectively. For the PBF-EB-manufactured Ti-6Al-4V in an as-built condition, other researchers have reported β phase volume fractions between 1% and 3%.[24,44] Furthermore, additional heat treatment increases the volume fraction of the β phase after heat treatment.[44] The increase in β phase volume fraction directly depends on the heat-treatment temperature. A study of Ti-6Al-4V produced by laser powder bed fusion using X-ray diffraction[45] reported β phase volume fractions of about 4%, 6%, and 8% after heat treatment at 770°C, 840°C, and 1008°C, respectively. In the present study, it has been observed that the material subjected to a higher HIP treatment temperature reported an increased β phase volume fraction.

One of the reasons for the increased volume fraction of the β phase after HIP treatment could be the difference in the cooling rate between the build process and the HIP treatment. In the PBF-EB build chamber, the material is cooled at a faster cooling rate between 10^3 K/s and 10^5 K/s.[4] The rapid transformation of $\beta \rightarrow \alpha$ occurs with limited time available for the β phase to attain an equilibrium state, resulting in diffusionless martensitic transformation during the initial melting cycle. Even though the martensite becomes decomposed during the subsequent remelting, the remelting temperature is below the β transus temperature. Consequently, a limited volume fraction of the β phase had been observed in the as-built condition. On the other hand, after HIP treatment, the material is cooled at a relatively slower cooling rate of 30 K/min,[9] providing sufficient time for the β phase to reach its equilibrium volume fraction. Therefore, the volume fraction of the β phase is reported to be higher for the HIP-treated materials. While the volume fraction of the β phase improves with the HIP treatment, the volume is comparatively lower than the volume fraction of the α phase to be detected efficiently by neutron diffraction.

It is essential to determine the load partitioning between constituent phases in a multiphase alloy to understand the impact on mechanical properties by respective phases. The load partitioning between the α and β phases, as shown in Fig. 8b, indicates that the β phase has been subjected to higher stresses during plastic deformation. As a result, the intergranular micro-stresses of the β phase between the α laths could be slightly higher at the α–β interface. The difference in phase micro-stresses could lead to anisotropic mechanical properties and the α–β interface could become more prone to crack initiation, as reported in other $\alpha + \beta$ titanium alloys.[46] In the future, micro-stresses in the α–β interface could be investigated through in situ tensile testing in SEM that may potentially reveal more insights into any anisotropic behaviour at these interfaces.

CONCLUSIONS

Neutron diffraction has been used to study the evolution of lattice strains and load partitioning in phases during tensile testing at 20°C and 350°C. The following conclusions were made:

- For both HIP-treated materials tested at 20°C, the basal plane {0 0 0 2} was activated first, followed by activation of the pyramidal plane {1 0 $\bar{1}$ 1}. On the other hand, load transfer occurred in the prismatic diffraction plane {1 0 $\bar{1}$ 0}.
- At 350°C, there were indications of the pyramidal plane {1 0 $\bar{1}$ 1} becoming activated and load transfer occurring in the basal {0 0 0 2} and prismatic {1 0 $\bar{1}$ 0} diffraction planes.
- The phase volume fraction calculated from the diffraction data indicated that the modified HIP-treated material had a higher volume fraction of α phase than the standard HIP-treated material.
- The load partitioning results indicate that the β phase withstands higher stresses than the α phase in the plastic regime, which could result in anisotropic mechanical properties and micro-stresses at the α-β interfaces.
- The EPSC model effectively predicted the strain evolution of the α phase in modified HIP-treated PBF-EB-manufactured Ti-6Al-4V to a close agreement with the experimental results.

ACKNOWLEDGEMENTS

The authors want to acknowledge the support from GE-Additive in providing the PBF-EB-manufactured material for this research. The help from Quintus Technologies AB for HIP treatment of the test samples is much appreciated. Finally, the authors would like to thank GKN-Aerospace and AIM for their continuous support. Financial support from VINNOVA, through the “Nationella flygtekniska forskningsprogrammet 7” (NFFP) (project #: 2019-02741), is highly appreciated. Part of the work done by Magnus Ekh has been funded by the Swedish Research Council (Vetenskapsrådet) under grant number 2018-06482. The neutron experiment at the Materials and Life Science Experimental Facility of the J-PARC was performed under a user program Proposal No. 2020B0124.

FUNDING

Open access funding provided by University West.

CONFLICT OF INTEREST

The authors declare no conflict of interest.

OPEN ACCESS

REFERENCES

1. R. Huang, M. Riddle, D. Graziano, J. Warren, S. Das, S. Nimbalkar, J. Cresko, and E. Masanet, *J. Clean. Prod.* 135, 1559 https://doi.org/10.1016/J.JCLEPRO.2015.04.109 (2016).
2. S. Liu and Y.C. Shin, *Mater. Des.* 164, 107552 https://doi.org/10.1016/J.MATDES.2018.107552 (2019).
3. A. Safdar, L.Y. Wei, A. Snis, and Z. Lai, *Mater. Charact.* 65, 8 https://doi.org/10.1016/J.MATCHAR.2011.12.008 (2012).
4. S.S. Al-Bermani, M.L. Blackmore, W. Zhang, and I. Todd, *Metall. Mater. Trans. A* 41, 3422 https://doi.org/10.1007/S11661-010-0397-X/FIGURES/13 (2010).
5. M. Neikter, PhD Thesis, Luleå University of Technology, Luleå, 2019.
6. X. Gong, T. Anderson, and K. Chou, *Manuf. Rev.* 1, 2 https://doi.org/10.1051/MFREVIEW/2014001 (2014).
7. S. Tammas-williams, P.J. Withers, I. Todd, and P.B. Prangnell, *Metall. Mater. Trans. A* 47, 1939 https://doi.org/10.1007/s11661-016-3429-3 (2016).
8. A. Mohammadhosseini, D. Fraser, S.H. Masood, and M. Jahedi, *Mater. Res. Innov.* 17, s106 https://doi.org/10.1179/1432891713Z.000000000302 (2013).
9. A. Eklund, M. Ahlfors, F. Bahbou, and J. Wedenstrand, *Key Eng. Mater.* 770, 174 https://doi.org/10.4028/www.scientific.net/KEM.770.174 (2018).
10. K.T. Pandian, M. Neikter, F. Bahbou, T. Hansson, and R. Pederson, *Materials* 15, 3624 https://doi.org/10.3390/MA15103624 (2022).
11. L. Facchini, E. Magalini, P. Robotti, and A. Molinari, *Rapid Prototyp. J.* 15, 171 https://doi.org/10.1108/13552540910960262 (2009).
12. G. Lütjering and J.C. Williams, *Titanium* (Springer, Berlin Heidelberg, 2007), pp19–23.
13. P.R. Dawson, D.E. Boyce, J.S. Park, E. Wielewski, and M.P. Miller, *Acta Mater.* 144, 92 https://doi.org/10.1016/J.ACTAMAT.2017.10.032 (2018).
14. C. Leyens and M. Peters, *Titanium and Titanium Alloys* (Wiley, 2003), pp5–6.
15. T.B. Britton, F.P.E. Dunne, and A.J. Wilkinson, *Proc. R. Soc. A* 471, 20140881 https://doi.org/10.1098/RSPA.2014.0881 (2015).
16. H. Conrad, M. Doner, and B. DeMeester, Titanium Sci. Technol., In : Proceedings of International Conference, 2nd, 969 (1972).
17. H. Li, D.E. Mason, T.R. Bieler, C.J. Boehlert, and M.A. Crimp, *Acta Mater.* 61, 7555 https://doi.org/10.1016/J.ACTAMAT.2013.08.042 (2013).
18. S. Zaefferer, *Mater. Sci. Eng. A* 344, 20 https://doi.org/10.1016/S0921-5093(02)00421-5 (2003).
19. P.A. Turner and C.N. Tome, *Acta Metall. Mater.* 42, 4143 (1994).
20. E.C. Oliver, M.R. Daymond, J. Quinta Da Fonseca, and P.J. Withers, *J. Neutron Res.* 12, 33 https://doi.org/10.1080/10238160410001734423 (2004).
21. D. Gloaguen, G. Oum, V. Legrand, J. Fajoui, M.J. Moya, T. Pirling, and W. Kockelmann, *Metall. Mater. Trans. A* 46, 5038 https://doi.org/10.1007/S11661-015-3073-3/FIGURES/9 (2015).
22. A.M. Stapleton, S.L. Raghunathan, I. Bantounas, H.J. Stone, T.C. Lindley, and D. Dye, *Acta Mater.* 56, 6186 https://doi.org/10.1016/J.ACTAMAT.2008.08.030 (2008).
23. K. Sofinowski, M. Šmíd, I. Kuběna, S. Vivès, N. Casati, S. Godet, and H. Van Swygenhoven, *Acta Mater.* 179, 224 https://doi.org/10.1016/J.ACTAMAT.2019.08.037 (2019).
24. M. Neikter, R. Woracek, C. Durniak, M. Persson, M.L. Antti, P. Åkerfeldt, R. Pederson, J. Zhang, S.C. Vogel, and M. Strobl, *MATEC Web Conf.* 321, 03021 https://doi.org/10.1051/MATECCONF/202032103021 (2020).
25. A. Pesach, E. Tiferet, S.C. Vogel, M. Chonin, A. Diskin, L. Zilberman, O. Rivin, O. Yeheskel, and E.A.N. Caspi, *Addit. Manuf.* 23, 394 https://doi.org/10.1016/J.ADDMA.2018.08.010 (2018).
26. M. Neikter, R. Woracek, T. Maimaitiyili, C. Scheffzük, M. Strobl, M.L. Antti, P. Åkerfeldt, R. Pederson, and C. Bjerkén, *Addit. Manuf.* 23, 225 https://doi.org/10.1016/J.ADDMA.2018.08.018 (2018).
27. S.C. Vogel, S. Takajo, M.A. Kumar, E.N. Caspi, A. Pesach, E. Tiferet, and O. Yeheskel, *JOM* 70, 1714 https://doi.org/10.1007/S11837-018-3038-2 (2018).
28. O. Muránsky, D.G. Carr, M.R. Barnett, E.C. Oliver, and P. Šittner, *Mater. Sci. Eng. A* 496, 14 https://doi.org/10.1016/J.MSEA.2008.07.031 (2008).
29. S.R. Agnew, C.N. Tomé, D.W. Brown, T.M. Holden, and S.C. Vogel, *Scr. Mater.* 48, 1003 https://doi.org/10.1016/S1359-6462(02)00591-2 (2003).
30. R. Oishi, M. Yonemura, Y. Nishimaki, S. Torii, A. Hoshikawa, T. Ishigaki, T. Morishima, K. Mori, and T. Kamiyama, *Nucl. Instrum. Methods Phys. Res. Sect. A* 600, 94 https://doi.org/10.1016/J.NIMA.2008.11.056 (2009).
31. R.A. Lebensohn and C.N. Tomé, *Acta Metall. Mater.* 41, 2611 https://doi.org/10.1016/0956-7151(93)90130-K (1993).
32. N. Jia, Z.H. Cong, X. Sun, S. Cheng, Z.H. Nie, Y. Ren, P.K. Liaw, and Y.D. Wang, *Acta Mater.* 57, 3965 https://doi.org/10.1016/J.ACTAMAT.2009.05.002 (2009).
33. H. Li, M. Ekh, M.H. Colliander, and F. Larsson, *Int. J. Plast.* 110, 248 https://doi.org/10.1016/J.IJPLAS.2018.07.006 (2018).
34. M.H. Yoo and C.T. Wei, *J. Appl. Phys.* 38, 4317 https://doi.org/10.1063/1.1709121 (1967).
35. E.D. Levine, *Trans. Metall. Soc. AIME* 236, 1558 (1966).
36. J.C. Williams, R.G. Baggerly, and N.E. Paton, *Metall. Mater. Trans. A* 33, 837 https://doi.org/10.1007/S11661-002-0153-Y (2002).
37. B.R. Anne, Y. Okuyama, T. Morikawa, and M. Tanaka, *Mater. Sci. Eng. A* 798, 140211 https://doi.org/10.1016/J.MSEA.2020.140211 (2020).
38. S.H. Wang, M.D. Wei, and L.W. Tsay, *Mater. Lett.* 57, 1815 https://doi.org/10.1016/S0167-577X(02)01074-1 (2003).
39. D.G.L. Prakash, R. Ding, R.J. Moat, I. Jones, P.J. Withers, J.Q.D. Fonseca, and M. Preuss, *Mater. Sci. Eng. A* 527, 5734 https://doi.org/10.1016/J.MSEA.2010.05.039 (2010).
40. J.M. Vallejos, P. Barriobero-Vila, J. Gussone, J. Haubrich, K. Kelm, A. Stark, N. Schell, and G. Requena, *Adv. Eng. Mater.* 23, 2001556 https://doi.org/10.1002/ADEM.202001556 (2021).
41. P. Wang, X. Tan, M.L.S. Nai, J. Wu, and J. Wei, *Mater. Sci. Eng. A* 833, 142568 https://doi.org/10.1016/J.MSEA.2021.142568 (2022).
42. J.W. Christian and S. Mahajan, *Prog. Mater. Sci.* 39, 1 https://doi.org/10.1016/0079-6425(94)00007-7 (1995).

43. K.E. Agbovi, B. Girault, J. Fajoui, S. Kabra, W. Kockelmann, P.A. Dubos, and D. Gloaguen, *JOM* 75, 3055 https://doi.org/10.1007/S11837-023-05840-4/FIGURES/8 (2023).
44. S. Takajo, T. Tomida, A.N. Caspi, A. Pesach, E. Tiferet, S.C. Vogel, O. Mishin, and S. Birosca, *Metals* 11, 1661 https://doi.org/10.3390/MET11101661 (2021).
45. D.W. Brown, V. Anghel, L. Balogh, B. Clausen, N.S. Johnson, R.M. Martinez, D.C. Pagan, G. Rafailov, L. Ravkov, M. Strantza, and E. Zepeda-Alarcon, *Metall. Mater. Trans. A* 52, 5165 https://doi.org/10.1007/S11661-021-06455-7/FIGURES/13 (2021).
46. Y. Cui, C. Li, S. Harjo, C. Zhang, R. Li, W. Zheng, and Y. Wang, *MATEC Web Conf.* 321, 11013 https://doi.org/10.1051/MATECCONF/202032111013 (2020).